SLAC-PUB-3408
August 1984
(A)

MODELING OF THE SLC ELECTRON DAMPING RING*

JOHANN JÄGER, MARTIN LEE, MARK WOODLEY
Stanford Linear Accelerator Center
Stanford University, Stanford, California 94305
and
JEAN-PIERRE DELAHAYE
CERN
Geneva, Switzerland

Introduction

The SLC electron Damping Ring has been in operation now for more than a year.[1] Operation of the Damping Ring during this running-in period has been a "fly by the seat of your pants" affair: optimization of operating parameters has been accomplished by trial-and-error adjustment of many power supplies, a very complicated and difficult task to say the least! This initial period of manual operation was needed, however, for debugging of both hardware and software tools and gave us much valuable operational experience.

The successful completion of the "10 Sectors" test in February 1984[2] marked the end of the era of manual operation of the Ring for two important reasons. First, although the "10 Sectors" test had demonstrated that a beam could be injected into the Ring, stored, damped and extracted with properties that conformed to SLC specifications, there was an obvious need to improve injection and extraction efficiency and to further optimize the equilibrium properties of the damped beam. Second, although the Ring had been designed to operate at an energy of 1.21 GeV, all running up until this point had been at the lower energy of 0.95 GeV due to the unavailability of beam from the injector at the design energy (SLED-I had not yet been implemented). Hence we were faced with the

* Work supported by the Department of Energy, contract DE-AC03-76SF00515

(Submitted for Publication)

prospect of re-measurement and re-optimization of the Ring parameters at the design energy, parameters which were expected to be quite different due to the fact that the magnetic elements of the Ring operate in a highly saturated state at 1.21 GeV. Compounding these problems were the time constraints imposed on us by the ambitious construction schedule for the SLC. Whereas we had taken nearly a year to measure and optimize the Ring parameters manually at the lower energy, we had only three months to repeat this process at the design energy in order that the experience gained could be applied to the finalization of the design of the positron Damping Ring which was soon to begin construction.

In order to make the most efficient use of the short time allotted to us it was therefore decided to undertake the re-measurement and re-optimization of the Ring at the design energy utilizing simulation model driven procedures which had been developed based on the experience acquired during the first year of Ring operation. During these last three months much has been accomplished through the application of these model driven procedures: beam has been injected and stored successfully at 1.21 GeV and most of the pertinent beam parameters have been measured and optimized.[3]

The purpose of this note is to describe both the evolution of the computer simulation model of the Damping Ring and some of the model driven procedures which have been developed for its operation and control, as well as to illustrate the use and effectiveness of some of these procedures with examples taken from Damping Ring operation.

1. The Original Model

The computer simulation model of the Damping Ring (to be referred to hereafter simply as "the model") consists of a data file containing the lengths and positions of all magnetic elements in the Ring combined with a computer program which is able to compute the optical properties of the Ring given the strengths of the magnetic elements or, conversly, to compute the strengths of the magnetic elements which yield a desired set of Ring optical properties.[4] The conversion of power supply currents into magnetic element strengths and vice versa is, as we shall see, an implicit and important part of any on-line control model.

The first Damping Ring model was the design lattice as created by H. Wiedemann[5] using the computer program MAGIC.[6] The lengths, strengths and placement of the magnetic elements in the original MAGIC data file were translated into a similar file for the computer program COMFORT[7] which was to be used for on-line control of the Ring. For given magnetic element strengths, beam injection energy and RF voltage COMFORT computes the lattice functions, beam sizes, damping rates, chromaticities, etc., or for some specified desired lattice function values COMFORT finds the corresponding magnetic element strengths. In addition, COMFORT computes the elements of the transfer matrices which relate changes in the closed orbit at any position monitor to unit kicks of the beam at any orbit corrector for a given configuration. A typical COMFORT data file for the Ring is shown in Fig. 1.

The Ring lattice consists of two symmetric superperiods. Within each superperiod there are eight standard FODO cells, two matching cells and two half-insertions. The Ring's magnetic elements consist of 40 wedge bends, 6 independent quad families and 2 sextupole families; in addition there are 26 horizontal and 14 vertical orbit correctors which consist of trim windings on 22 bend magnets and 18 quads. Diagnostic devices in the Ring include 26 beam position monitors, a synchrotron light monitor, movable scrapers and a tune monitor. The placement of the magnetic elements in the Ring is illustrated in Fig. 2.

Chromaticity correction in the Ring, necessary for control of the head-tail instability, is accomplished with the two families of real sextupoles and with positive and negative sextupole fields introduced at each end of the bends by means of appropriately shaped pole-end pieces. In addition, the bend magnets are made "wedge" by rotation of these pole-end pieces. Figure 3 shows a schematic representation of the Ring bend magnet; the pole-piece which has a focusing sextupole field is called a "hole" while the pole-piece which has a defocusing sextupole field is called a "nose.". The strengths of the Ring's magnetic elements were chosen in the design[8] for a lattice characterized by the following machine function values ("$*$" indicates values at the symmetry point at the center of the injection straight section):

$$\beta_x * = 4.40m$$
$$\beta_y * = 0.53m$$
$$\eta_x * = 0.0m$$

$$\alpha_x = 0.0$$
$$\alpha_y = 0.0 \qquad \text{(start of FODO cells)}$$
$$\eta_x' = 0.0$$

$$\nu_x = 7.2$$
$$\nu_y = 3.2$$

A plot of the machine function values for this lattice is shown in Fig. 4.

Results of measurement of the Ring magnets as constructed necessitated the updating of this original design model. New effective lengths were computed for the quads and bends and polynomials relating current to magnetic field in each magnet family were generated. The original design model, together with these updates, formed our first working model of the Ring.

Initial attempts to use this first working model for operation and control of the Ring met with repeated failure; modeling was temporarily abandoned in favor of "look and adjust" manual operation which led to stored beam in the Ring in late February 1983. The failure of the modeling during this early operation of the Ring can be attributed, at least in part, to problems with the hardware: 6 out of 26 beam position monitors, in the critical insertion and extraction regions where beta values are large, were inoperative; compensating coils on the septa were not effective in cancelling their highly non-linear leakage fields which led to orbit-dependent focusing and steering effects; corrector trim winding calibrations were uncertain due to saturation effects in the quads and bends; the tune measurement system was crude and inaccurate.

A considerable amount of data on the properties of the Ring was accrued in the remainder of its first running cycle, which ended with the summer Linac shutdown in May 1983. As we will see, the most useful information for the modelers was contained in what we call "bump" measurements: the measured changes in closed orbit due to known kicks introduced at the various correctors.

2. The Empirical Model

The focusing effects seen by the beam at the entrance and exit edges of one of the bend magnets may be represented by equivalent pole-face rotation angles, one for the "nose" and one for the "hole." Figures 5 and 6 show that the actual edge angle seen by the beam depends, rather strongly in the case of the "noses," on the horizontal position of the beam with respect to the centerline of the pole-piece. Since detailed information on the position of the beam at each of the pole-end pieces was not available, it was decided to average these effects around the Ring by using a single pole-face angle to represent the focusing effects of each of the "noses" and another for each of the "holes." The model can then be made to simulate the real Ring in the following way: the actual current running in each magnet string is read out and its field/current polynomial used to get the model magnet strengths; the two pole-face angles are then varied to bring the model tunes into accord with the measured tunes. Analysis of the "bump" mesasurements during the summer using the above trick led to the development of a new Ring model dubbed the "Empirical" model.

Figure 7 shows a typical "bump" measurement (vertical plane) along with the first working model's prediction of the orbit which would result from the given corrector kick. We noted that in all cases the fit between the measured and predicted orbits was good in the horizontal plane but obviously not very good in the vertical plane; we quantified this "goodness of fit" with a number which we call the RMS-ratio. The RMS-ratio is defined to be the ratio of the RMS of the difference between the predicted and measured orbit values to the RMS of the measured orbit values. Given the resolution of our position monitor readings (around 200 microns), a "good" value for the RMS-ratio would be 0.2. Figure 8 shows the RMS-ratio values for 12 vertical and 8 horizontal "bump" measurements. It shows that the first working model was able to predict the "bump" orbits fairly well in the horizontal plane but that it had real problems in the vertical plane.

Our next step was to introduce random errors in the strengths of each of the six quadrupole families, using the two variable pole-face angles to keep the model tunes and the measured tunes equal. A search was made in this way to find a

single quadrupole family error which would minimize the RMS-ratio values for all cases. We found that the only error we could introduce which would give us good agreement between measurement and prediction in both planes was a -3% error in the QDI quadrupole family (the four vertically focusing quadrupoles in the insertion and extraction regions). Figures 9 and 10, when compared to Figs. 7 and 8, illustrate the improvment in the model's ability to predict with this error in the QDI family. But is this error reasonable? Figure 11 shows the magnetic measurement data for the QDI quads along with the third order polynomial used to characterize their field vs current behavior. We see that there are many data points in the 1.21 GeV design operating region, but that there are no data in the 0.95 GeV region where we were actually operating. The strength of the QDI's according to the polynomial at the 0.95 GeV operating current of 72 Amps is marked on the plot along with the strength corresponding to a -3% error in the polynomial at this current. We see that the polynomial "sags" in the 0.95 GeV region in order to fit the surrounding data points with a smooth curve; the -3% value can be obtained by the simple and reasonable procedure of interpolating between the surrounding data points along a straight line. Seeing that the -3% QDI error was not unreasonable, we then combined the first working model with the two variable pole-face angles and the -3% QDI error to form the Empirical model.

3. Model Driven Procedures

While work on the Empirical model was going on, several procedures were being developed for measurement and control of the Ring which would be based on a trustworthy simulation model. These procedures are summarized briefly below:

Change Configuration: changing the Ring's operating point on the tune diagram is facilitated with this procedure. Fitting constraints are inserted into the COMFORT input file which force quadrupole family strengths to be computed which yield the desired values of ν_x and ν_y while keeping the beta and eta functions periodic through the FODO cells and minimizing the value of η_x^*.

Scan Orbit: this procedure controls measurement of the closed orbit in the Ring. The user specifies the number of measurements to be made at each monitor per scan; if more than one measurement per scan is specified statistics are generated for each monitor. In addition to simple absolute orbit scans, provision has been made to enable the user to save an orbit scan and to specify that subsequent scans are to be the difference between the absolute orbit and the saved orbit (this is how "bump" measurements are made). Also included is the ability to store orbit scans on disk for off-line analysis and to eliminate "bad" monitors.

Correct Orbit: given an orbit scan, this procedure computes corrector kicks which minimize the RMS of the residual orbit values after correction. Solutions which use from one to seven correctors, along with predicted residual orbits, are calculated using corrector/monitor transfer matrices generated by the model; experience has shown that the correctors begin "fighting" each other when more than three or four are used to correct a given orbit. The user may also specify a subset of the available correctors to be used for correcting a given orbit.

Check Monitors: this procedure is used to find "bad" beam position monitors by analyzing the ability to correct measured orbits. Untrustworthy monitors are identified by correction of identical orbits from which each monitor, in turn, has been deleted. Deletion of a "bad" monitor usually results in a substantial improvment in the RMS of the predicted residual orbit after correction.

Calibrate Corrector: the orbit changes produced by applying a known current to a given corrector are scanned and the orbit extant before powering this corrector is subtracted off. The orbit correction procedure is then used to select the single corrector which best reduces the RMS of the resultant orbit. When the model is right, the corrector which was actually used is always chosen and the kick computed to correct the difference orbit may be combined with the known current in the corrector to yield a rough angle/current calibration.

Local Bumps: this procedure allows the user to vary the position and/or angle of the beam at the insertion or extraction septum without changing the orbit elsewhere in the Ring. The user chooses four correctors which will be used to make the local bump. The control software is then used to assign all four correctors to a single adjustable knob; when the knob is turned, the correctors

are powered in proportions calculated by the model to yield the desired "flavor" of bump (X or Y; angle or position) at the specified septum while keeping the orbit unchanged outside the section of the Ring encompassed by the four chosen correctors.

Ramp Energy: this procedure allows the user to change the energy of the Ring without changing configuration. The present Ring energy and the strengths of all magnets are first read out. The control software is then used to assign all Ring magnets to a single adjustable knob; when the knob is turned the Ring energy is changed incrementally by scaling all magnet strengths linearly by the ratio of the new energy to the old energy (note that it is the strengths of the magnets and not their currents which are scaled; the field/current polynomials are used to convert strength to current in order to properly compensate saturation effects).

Update Model: inspired by the development of the Empirical model, this procedure first reads out the strengths of the magnets in the Ring; the user is then prompted for the measured tune values associated with these magnet strengths and any magnet family calibration errors (such as the -3% error in the QDI family). The model values of the two variable pole-face angles are then adjusted to bring the model tunes into agreement with the measured tunes; this updated model is then used for Ring operation and control.

4. Applications

The end of the "10 Sectors" test in February 1984 marked the beginning of a three month period of machine physics studies at the Damping Ring in which the Empirical model and the procedures outlined above were used first to improve the operational characteristics of the Ring at 0.95 GeV and then to bring the Ring up to its design operating energy of 1.21 GeV while maintaining these improvments.

The UPDATE MODEL and CHANGE CONFIGURATION procedures were used to implement a pre-calculated configuration[9] at 0.95 GeV which was expected, based on model calculations, to reduce the equilibrium emittances in the Ring. Measurement of the emittances on the Synchrotron Light Monitor once this configuration had been established confirmed our expectations. Problems with beam lifetime and RF-aperture (how far one can swing the Ring RF fre-

quency away from its nominal operating frequency of 714 MHz without losing beam) in this configuration were overcome by correcting the equilibrium vertical orbit. Figure 12 shows typical SCAN ORBIT results both before and after using the CALIBRATE CORRECTOR and CORRECT ORBIT procedures. Correcting the vertical orbit increased beam lifetime in the Ring from approximately 20 minutes to more than two hours; the RF aperture was opened up from $\pm$50 KHz before correction to the full operating range of the RF system ($\pm$200 KHz) after correction.

Dramatic increases in injection efficiency were gained by fine tuning the injection trajectory with the LOCAL BUMPS procedure. Figure 13 shows SCAN ORBIT results ("difference" mode) for two examples of local bumps at the injection septum. By moving the stored beam away from the injection septum with a local horizontal bump we were able to turn off both the injection septum and its compensating backleg winding without losing the stored beam. Comparison of the tunes and closed orbits of this "bare" Ring with those measured when the septum and backleg were on enabled us to empirically determine the current needed in the backleg winding to completely cancel the leakage fields of the septum. It was discovered that 60 Amps was needed in the backleg for complete compensation, rather than the 40 Amps suggested by the septum designers; removal of the non-linear effects of the septum on the injecting beam yielded further improvments in injection efficiency.

In order to prepare for 1.21 GeV injection we used the RAMP ENERGY procedure to ramp a stored beam injected into this optimized configuration at 0.95 GeV up to the design energy of 1.21 GeV. Using the UPDATE MODEL procedure on the ramped configuration showed that, as expected, the -3% model error in the QDI quadrupole family was no longer necessary at 1.21 GeV. Figure 11 shows that there are many magnetic measurement data points for the QDI family in the region of 1.21 GeV, hence one would expect the field/current polynomial for this family to be much more accurate at this energy. In this way we were able to establish a working configuration for the Ring at 1.21 GeV before the high energy SLED-I beam was available from the injector.

When 1.21 GeV beam became available from Sector 1 we were able to inject and store beam immediately using the ramped configuration, leaving us more time to study the properties of the Ring at this energy. In the course of these studies a very low emittance configuration was found by manual adjustment of two Ring quadrupole families; however, the beam lifetime was very short and the injection efficiency poor in this "knobbed" configuration. Figure 14 shows the reason for these problems: the "knobbed" configuration left the Ring lattice badly mismatched. These problems were solved by application of the CHANGE CONFIGURATION procedure, yielding a nicely matched configuration as shown in Fig. 15. The points marked on the lower η function plot of Figure 15 are measured values, illustrating the good agreement which we now have between the model and the real Ring.

Another problem in the Ring which was spotted and diagnosed with our orbit fitting and correcting procedures was anamolous X/Y coupling. Figure 16 shows SCAN ORBIT results ("difference" mode) in both planes for an orbit distortion introduced by powering the extraction kicker magnet. Although the extraction kicker steers the beam in the horizontal plane only, we can see that the horizontal orbit distortion caused by the kicker couples rather strongly into the vertical plane near the 20 meter point in the Ring. In order to study this effect we made a series of horizontal bump measurements around the Ring and used the CORRECT ORBIT procedure to fit the resultant vertical orbit changes with dipole kicks at each of the Ring quadrupoles. Once again it was the QDI magnets which were found to be the most likely source for the coupling effects observed. By taking the horizontal offsets in the QDI's due to the horizontal bump and the vertical kicks at the QDI's predicted by the CORRECT ORBIT procedure it is possible to estimate an effective angular (rotational) error in the QDI quads which could account for the observed effects. The results of these calculations indicated that the QDI poles were effectively rotated by angles of 4-12 mrad. Unfortunately, earlier measurements of these magnets had not included measurements of their skew quadrupole components and so the coupling effects took us by surprise. In response to our prediction a measurement of the QDI's was made in which skew quadrupole components were specifically sought. Rotational errors of the predicted magnitude in the alignment of the poles of these quads

were indeed found; replacement and realignment of the poles in these magnets is now underway.

The results of the measurements of the Ring's properties at the design energy will be presented in seperate publications by the people who actually carried out those measurements. Work in the modeling group is now focused on integrating our model driven procedures into a standardized on-line control package for everyday Ring operation.

Acknowledgments

It is a pleasure to acknowledge the dedicated efforts of the many people who have contributed to the development of the Damping Ring model and to its (ongoing) incorporation into the SLC control system. In particular we wish to thank Helmut Wiedemann, Gerry Fischer and Ted Fieguth for their work in the development of the model, and Nan Phinney for her patient help in getting some of our model driven procedures on line. In addition, we would like to thank Gary Brown, Greg Hall, John Dawes and George Bell for their work in the lengthy data analysis which led to the development of the Empirical model, and Lenny Rivkin, Andrew Hutton and John Sheppard for their useful suggestions and support.

References

1. G. E. Fischer, W. Davies-White, T. Fieguth and H. Wiedemann, "A 1.21 GeV Damping Ring for the Stanford Linear Collider," SLAC-PUB-3170, July 1983.
2. J. C. Sheppard, *et al,* "Acceleration of High Charge Density Electron Beams in the SLAC Linac," SLAC-PUB-3284, January 1984.
3. L. Z. Rivkin, J.-P. Delahaye. Results to be published.
4. J. C. Sheppard, R. H. Helm, M. J. Lee and M. D. Woodley, "On-line Control Models for the Stanford Linear Collider," SLAC-PUB-3072, March 1983.
5. M. D. Woodley, M. J. Lee and H. Wiedemann, "A MAGIC data set for the Damping Ring," CN-169, April 1982.

6. A. S. King, M. J. Lee and W. W. Lee, "MAGIC, a Computer Code for Design Studies of Insertions and Storage Rings," SLAC-183, August 1975.

7. M. D. Woodley, M. J. Lee, J. Jäger and A. S. King, "Control of Machine Functions or Transport Systems," SLAC-PUB-3086, March 1983.

8. H. Wiedemann, "Parameters for the Damping Rings," CN-58, May 1981.

9. J.-P. Delahaye. Private communication.

Figure Captions

Fig. 1 A typical COMFORT dataset for the Damping Ring.

Fig. 2 Arrangement of magnetic elements in the Damping Ring.

Fig. 3 Schematic of Damping Ring bend magnet illustrating shape and orientation of pole pieces used for sextupole correction.

Fig. 4 Machine functions for the design Damping Ring lattice.

Fig. 5 Effective pole-face angle at "nose" face of Damping Ring bend magnet as a function of the horizontal offset of the beam from the centerline of the "nose"; dotted line shows the physical contour of the "nose".

Fig. 6 Effective pole-face angle at "hole" face of Damping Ring bend magnet as a function of the horizontal offset of the beam from the centerline of the "hole"; dotted line shows the physical contour of the "hole."

Fig. 7 Measured and predicted vertical closed orbit distortion in the Damping Ring due to a kick from a corrector located near monitor No. 11; the curves illustrate the discrepancy between the predictions of the first working model and measurements.

Fig. 8 RMS ratios (see text) for several "bump" measurements in the Damping Ring using the first working model; the large RMS ratio values for the vertical plane indicate poor agreement between measurement and model prediction.

Fig. 9 Measured and predicted vertical closed orbit distortion in the Damping Ring due to a kick from a corrector located near monitor No. 11; the predicted orbit comes from the Empirical Model of the Ring.

Fig. 10 RMS ratios (see text) for several "bump" measurements in the Damping Ring using the Empirical Model; compare with Fig. 8 to see the improvment in the model's ability to predict orbits.

Fig. 11 Magnetic measurement data and fitted third order polynomial for the Ring QDI quadrupole family; commissioning and initial operation of the Damping Ring was carried out at 950 MeV, far from any measured data points.

Fig. 12 Typical vertical closed orbit in the Damping Ring before and after using the CORRECT ORBIT procedure (Empirical Model).

Fig. 13 Local bumps introduced into the Damping Ring vertical closed orbit using the LOCAL BUMPS procedure (Empirical Model).

Fig. 14 Machine functions predicted by the Empirical Model for an experimentally discovered ("knobbed") Damping Ring configuration; note the mismatch in the vertical beta function.

Fig. 15 Machine functions predicted by the Empirical Model for the Damping Ring after applying the CHANGE CONFIGURATION procedure to the mismatched lattice of Fig. 14; the tunes are the same as in Fig. 14 and the beta functions are properly matched.

Fig. 16 Damping Ring trajectories due to a kick at the (horizontal) extraction kicker showing the coupling of the horizontal motion into the vertical plane in the vicinity of one of the QDI quadrupoles.

```
NUM         NSTP CONV
            1    10
    *       P0
            1.21359
DRF *       D0          D1          D2          D3          D4A
            1.0267      0.1473      0.1516      0.1067      0.3337
    *       D4B         D5          DQD         DQF
            0.4302      0.0962      0.0977      0.0962
BBX *       B
            0.0000
            0.3200
            9.0000
EDG *       EF          ED
            -3.29017    -13.85526
QUA *       QFH         QDH         QFIH        QDIH        QFMH
            -15.39459   19.97782    -10.58593   15.58019    -12.82584
            0.0828      0.0493      0.0843      0.0684      0.0828
    *       QDMH
            -0.60229
            0.0493
FIT         MCEL KICK
RPL  FBD    EF   B     ED
     DBF    ED   B     EF
     QFI    QFIH QFIH
     QDI    QDIH QDIH
     QFM    QFMH QFMH
     QDM    QDMH QDMH
            This lattice represents the first order magnetic
            elements for 1/4 of the Damping Ring.
CEL H       D0   QFI  D1   QDI  D2   FBD  D3   QDM
            D4A  KICK D4B  QFM  D5   FBD  DQD  QDH
            QDH  DQD  DBF  DQF  QFH
            QFH  DQF  FBD  DQD  QDH
            QDH  DQD  DBF  DQF  QFH
            QFH  DQF  FBD  DQD  QDH
            QDH  DQD  DBF  DQF  QFH
            QFH  DQF  FBD  DQD  QDH
            QDH  DQD  DBF  DQF  QFH  MCEL
            QFH  DQF  FBD  DQD  QDH
VAR         QFH  QDH  QFIH QDIH QFMH QDMH
FUN *BEG    BX          BY          EX
            1.0         1.0         1.0
            4.40000     0.53000     0.00000
FUN *FIT    NUX
            1.0
            0.25000
FUN *FIT    AX          AY          EXP
            1.0         1.0         1.0
            0.00000     0.00000     0.00000
FUN *END    NUX         NUY
            1.0         1.0
            0.80000     0.80000
PAR         NBML A      H    V
            4    1.0    84   0.80
FIN
```


4887A1

Fig. 1

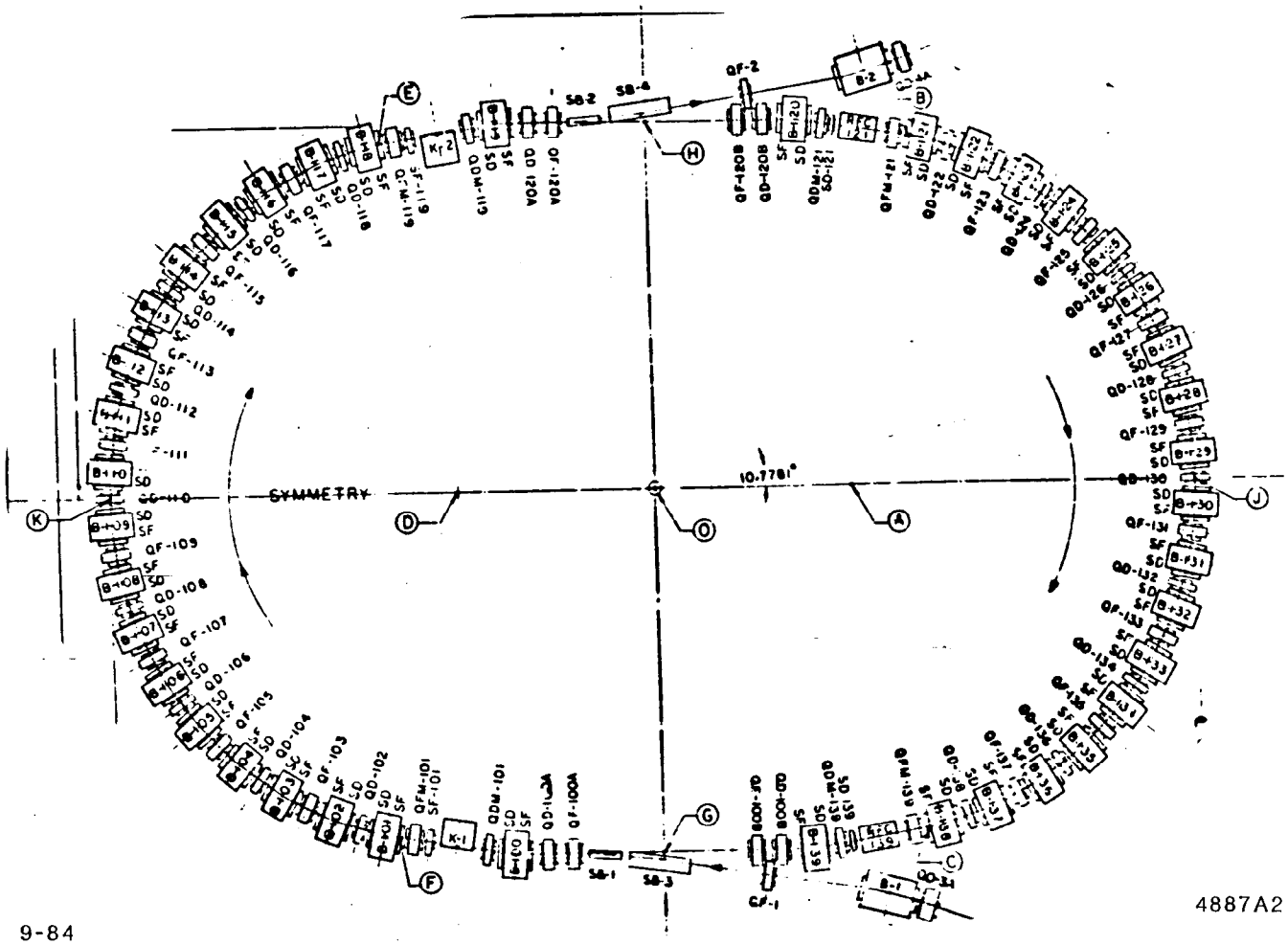
SYMMETRY
10.7781°
QF-2
SB-4
SB-2
SB-1
SB-3
QF-1
K-1
K-2
B-1
B-2
A
B
C
D
E
F
G
H
J
K
O
4887A2
9-84

Fig. 2

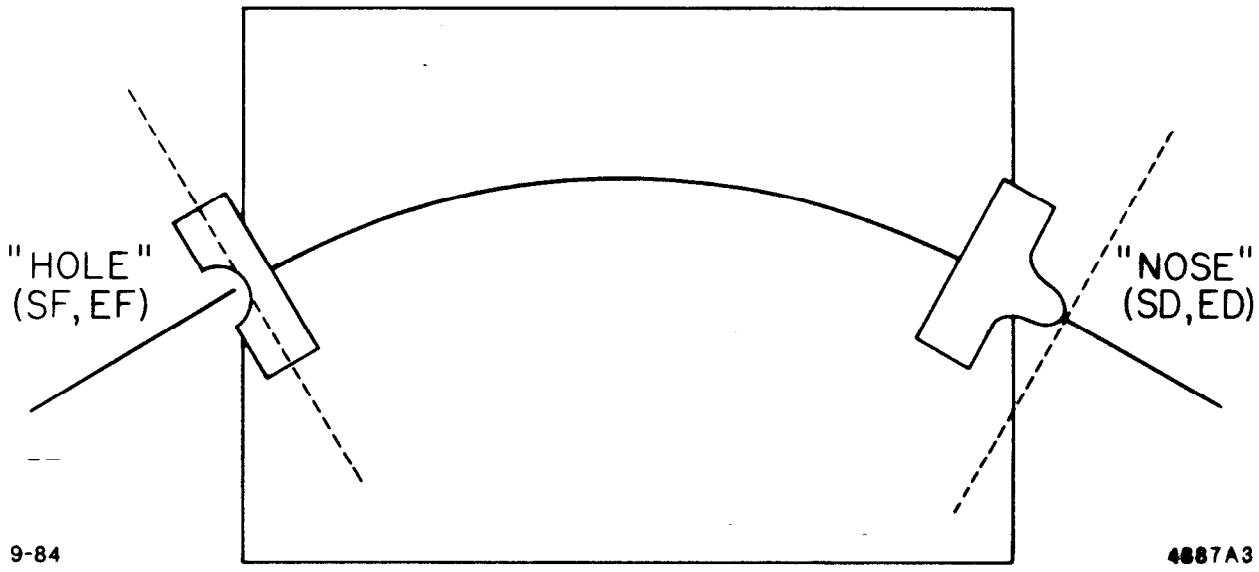

Fig 3

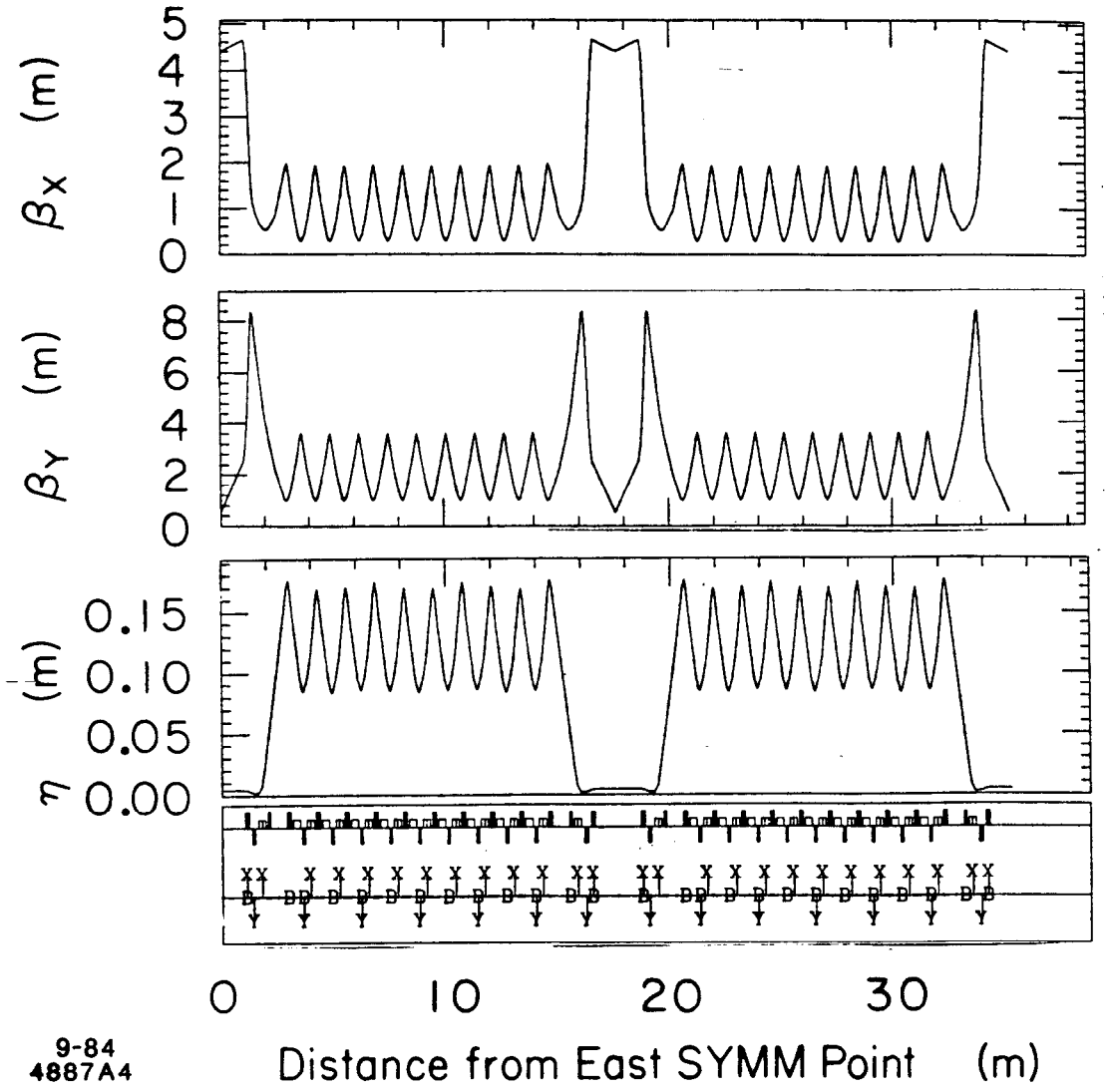
β_X (m)
5
4
3
2
1
0
β_Y (m)
8
6
4
2
0
η (m)
0.15
0.10
0.05
0.00
0
10
20
30
9-84
4887A4
Distance from East SYMM Point (m)

Fig. 4

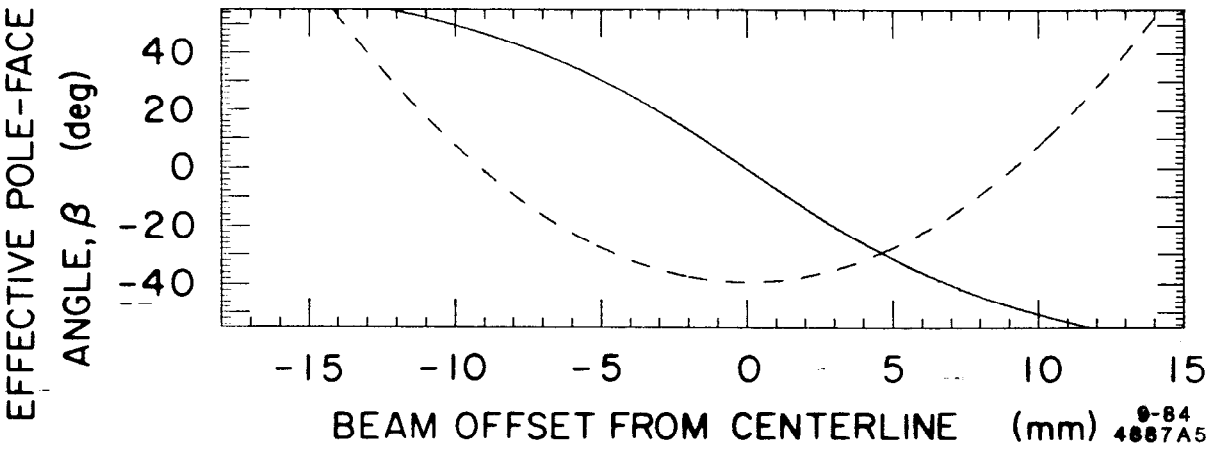
EFFECTIVE POLE-FACE ANGLE, β (deg)
40
20
0
-20
-40
-15
-10
-5
0
5
10
15
BEAM OFFSET FROM CENTERLINE (mm)
9-84
4887A5

Fig. 5

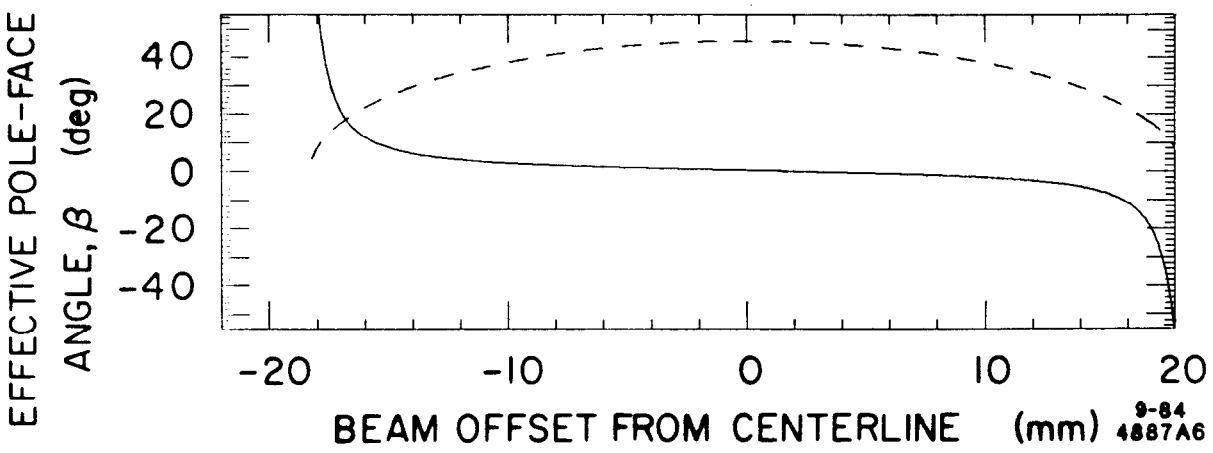
EFFECTIVE POLE-FACE ANGLE, β (deg)
40
20
0
-20
-40
-20
-10
0
10
20
BEAM OFFSET FROM CENTERLINE (mm)
9-84
4887A6

Fig. 6

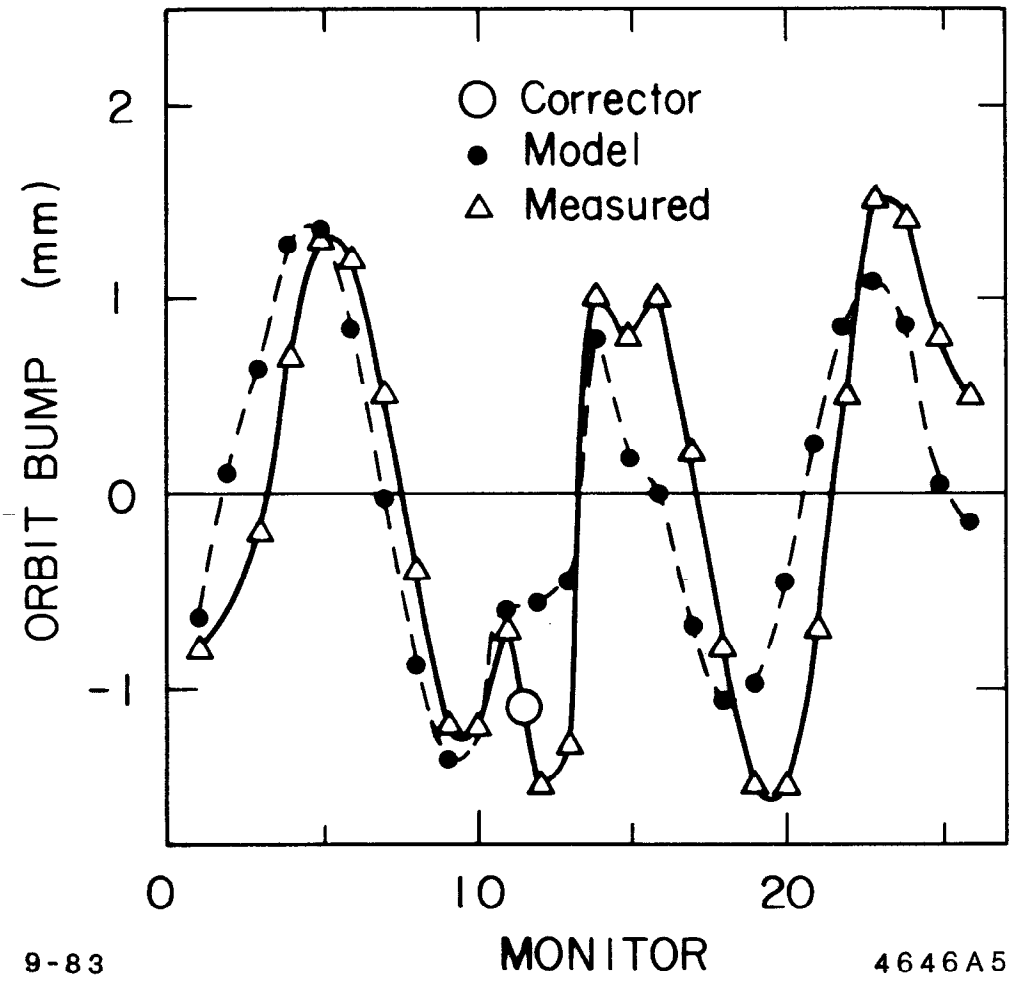
Corrector
Model
Measured
ORBIT BUMP (mm)
2
1
0
-1
0
10
20
MONITOR
9-83
4646A5

Fig. 7

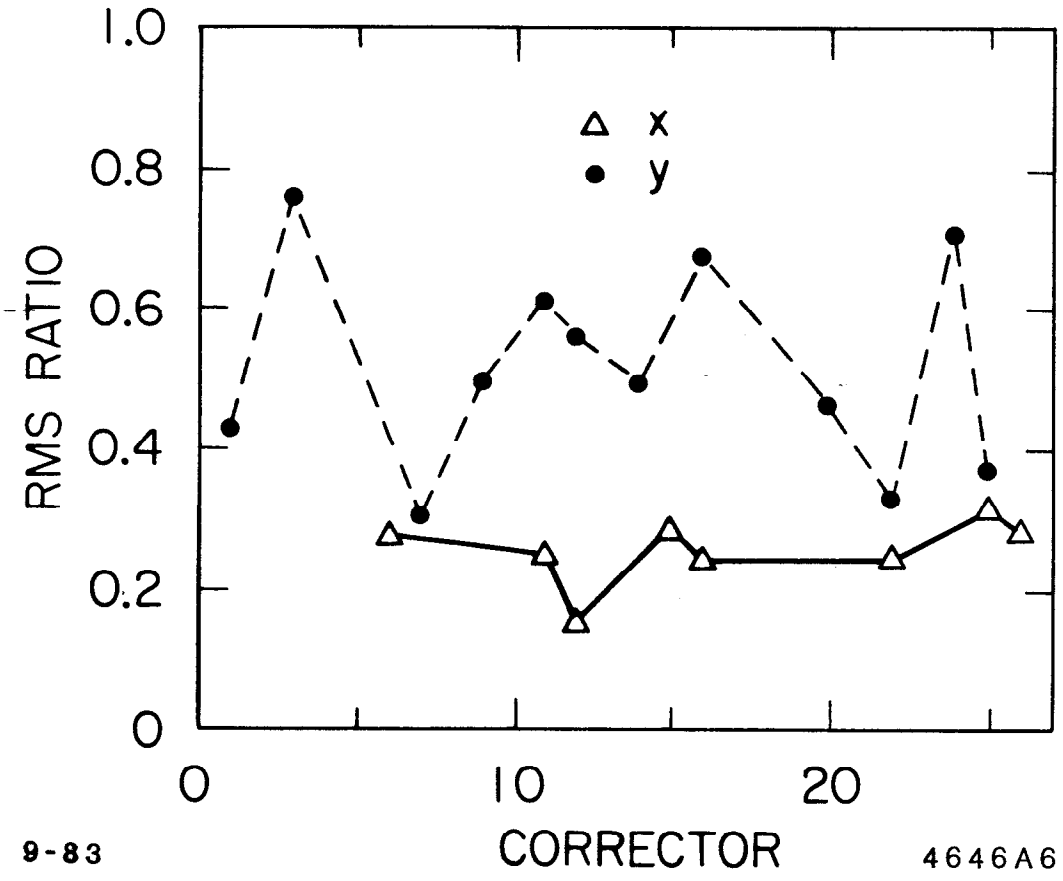

Fig. 8

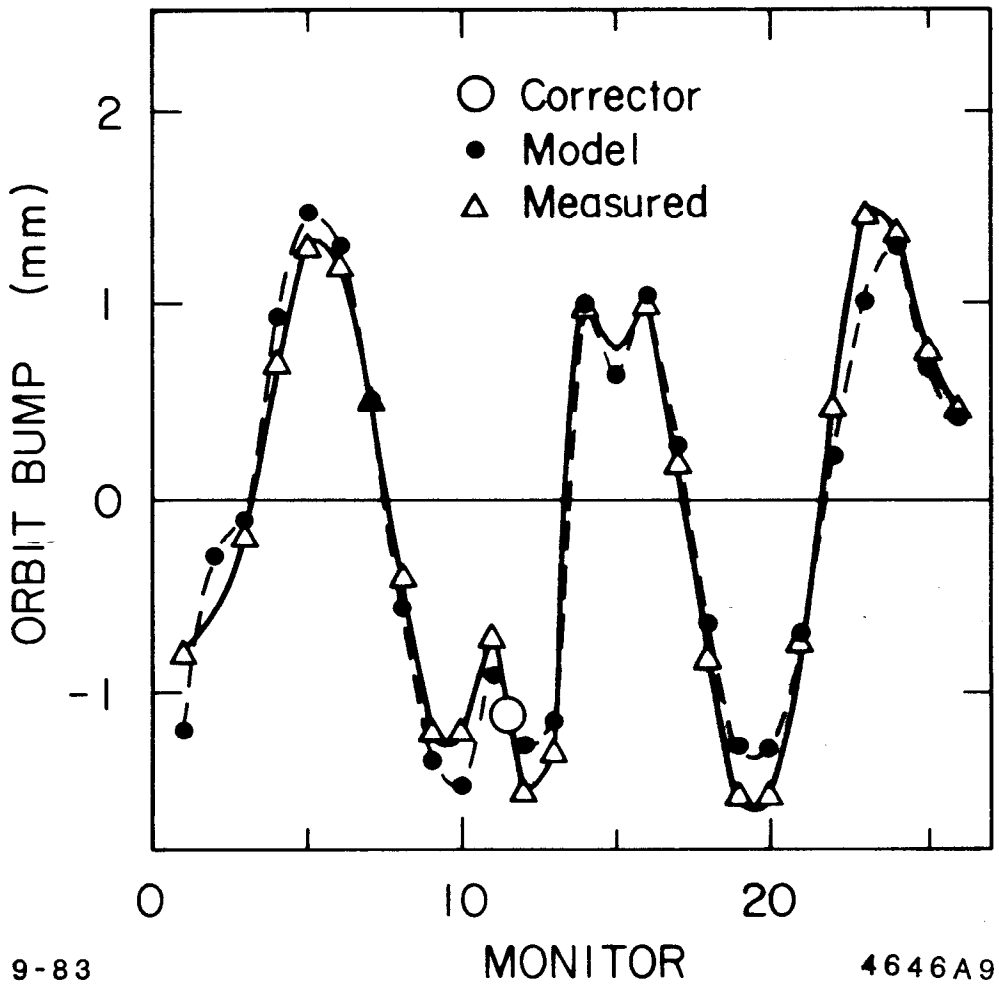
Corrector
Model
Measured
ORBIT BUMP (mm)
2
1
0
-1
0
10
20
MONITOR
9-83
4646A9

Fig. 9

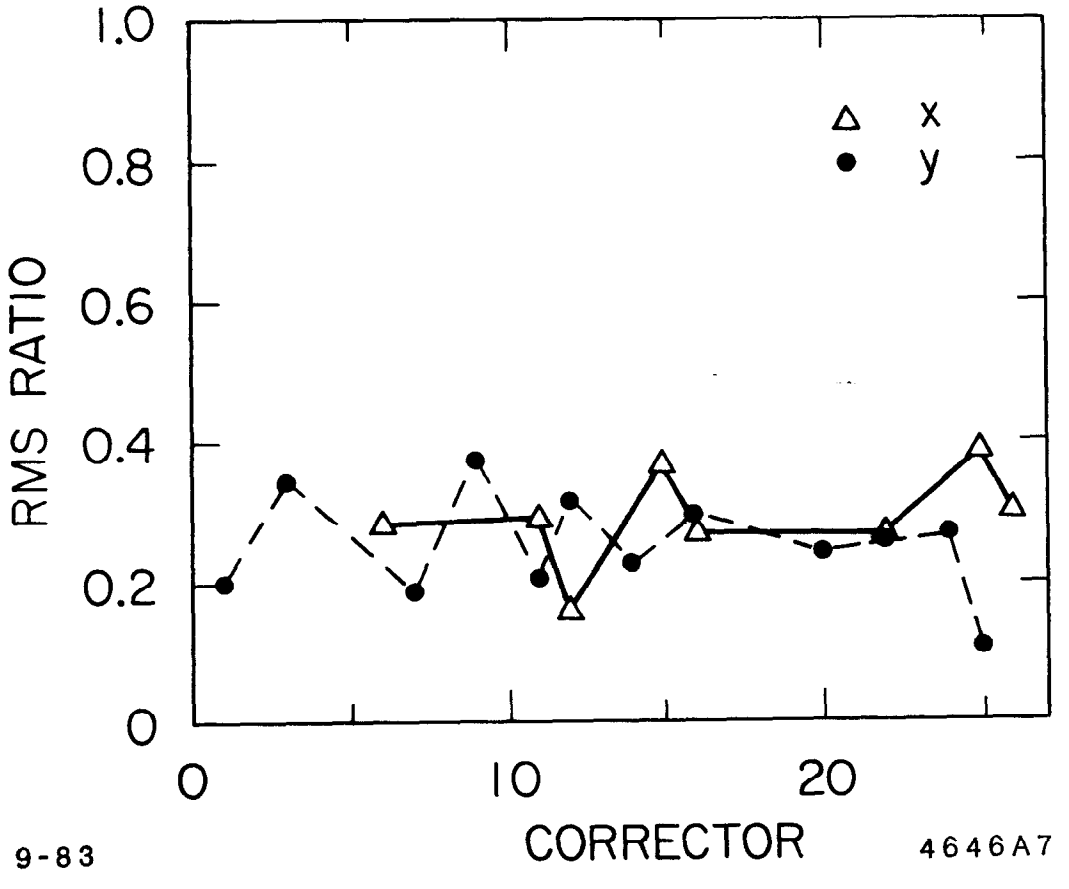

Fig. 10

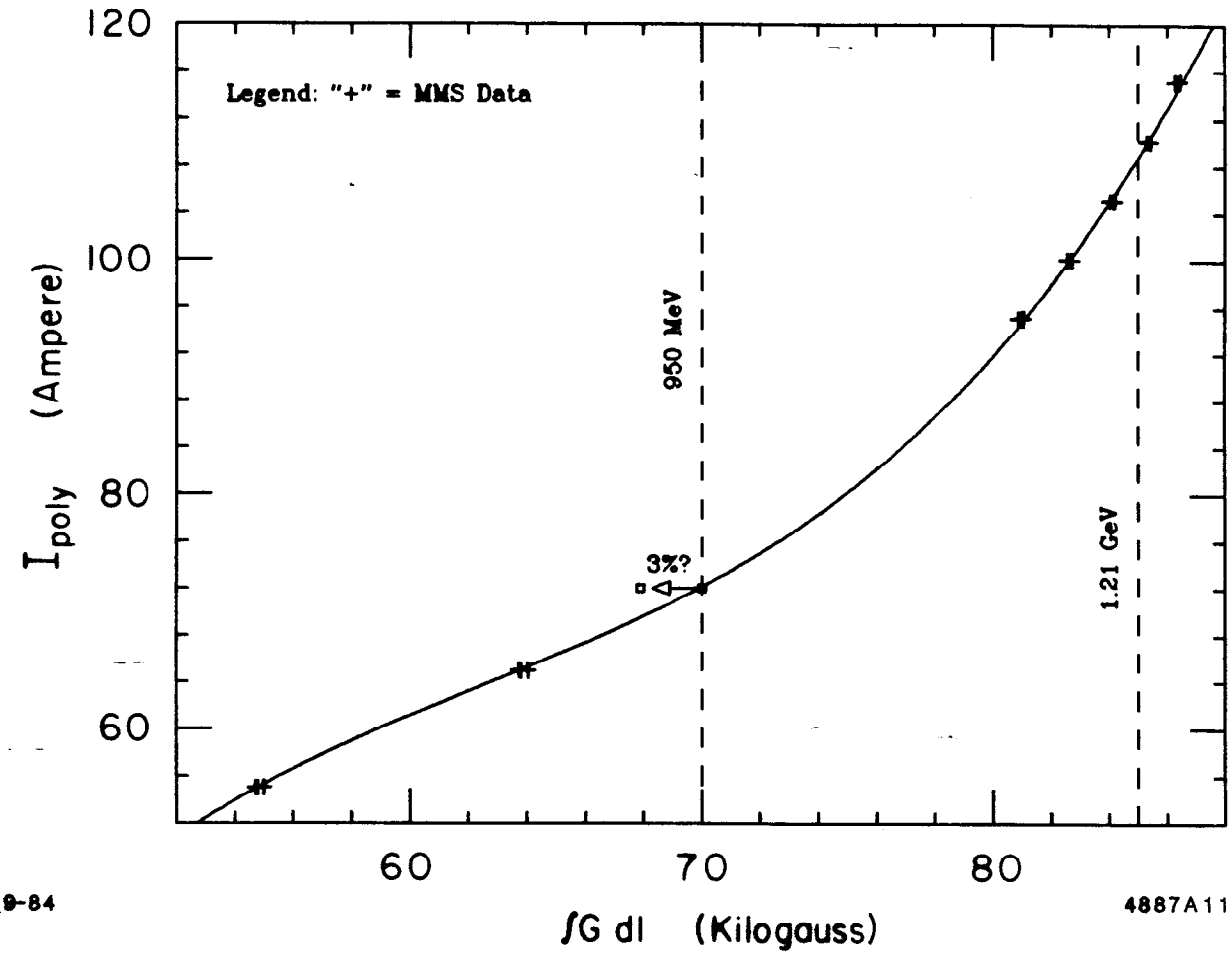
120
100
80
60
Legend: "+" = MMS Data
950 MeV
1.21 GeV
3%?
I_{poly} (Ampere)
60
70
80
∫G dl (Kilogauss)
9-84
4887A11

Fig. 11

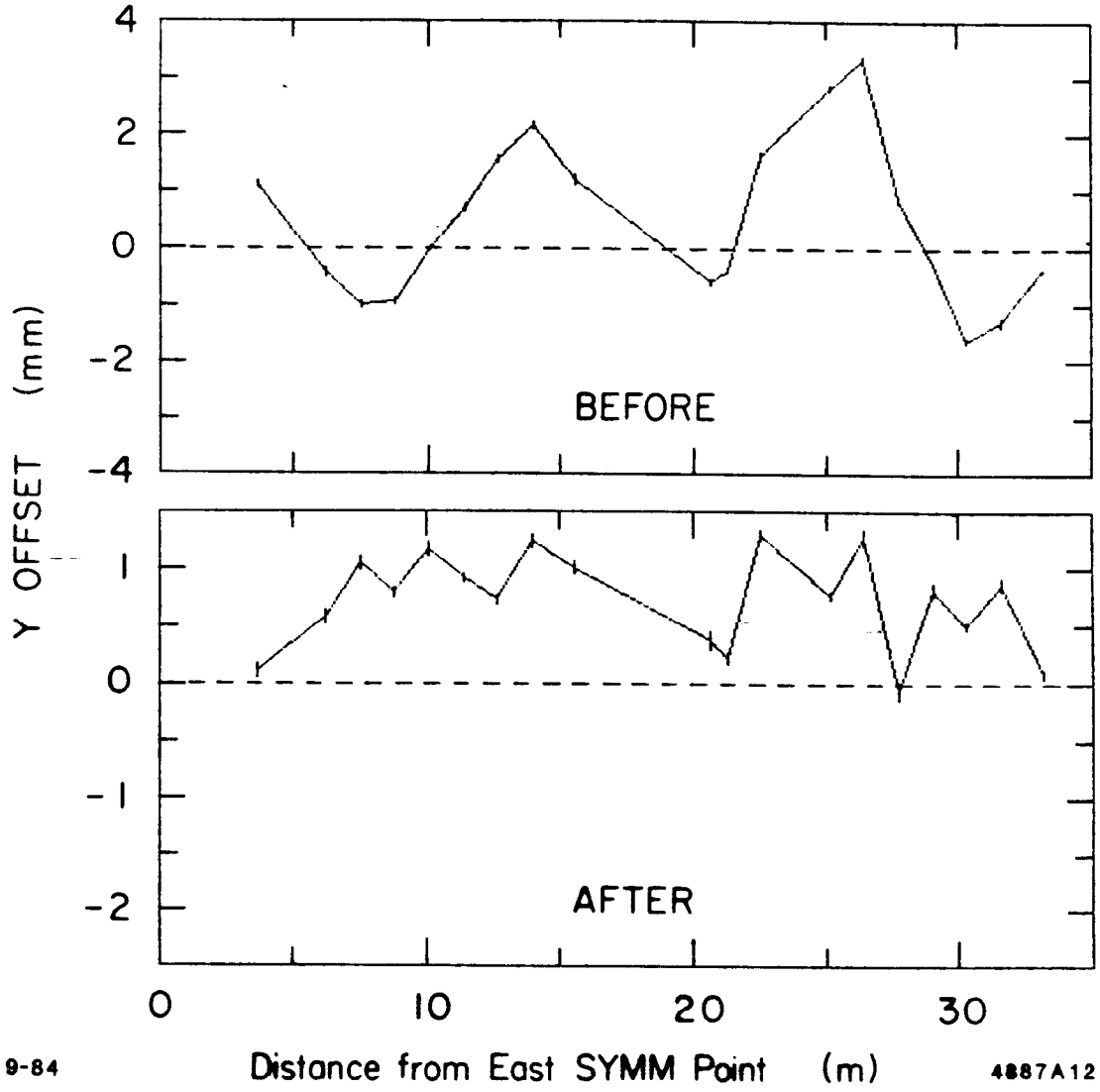
4
2
0
-2
-4
BEFORE
1
0
-1
-2
AFTER
Y OFFSET (mm)
0
10
20
30
Distance from East SYMM Point (m)
9-84
4887A12

Fig. 12

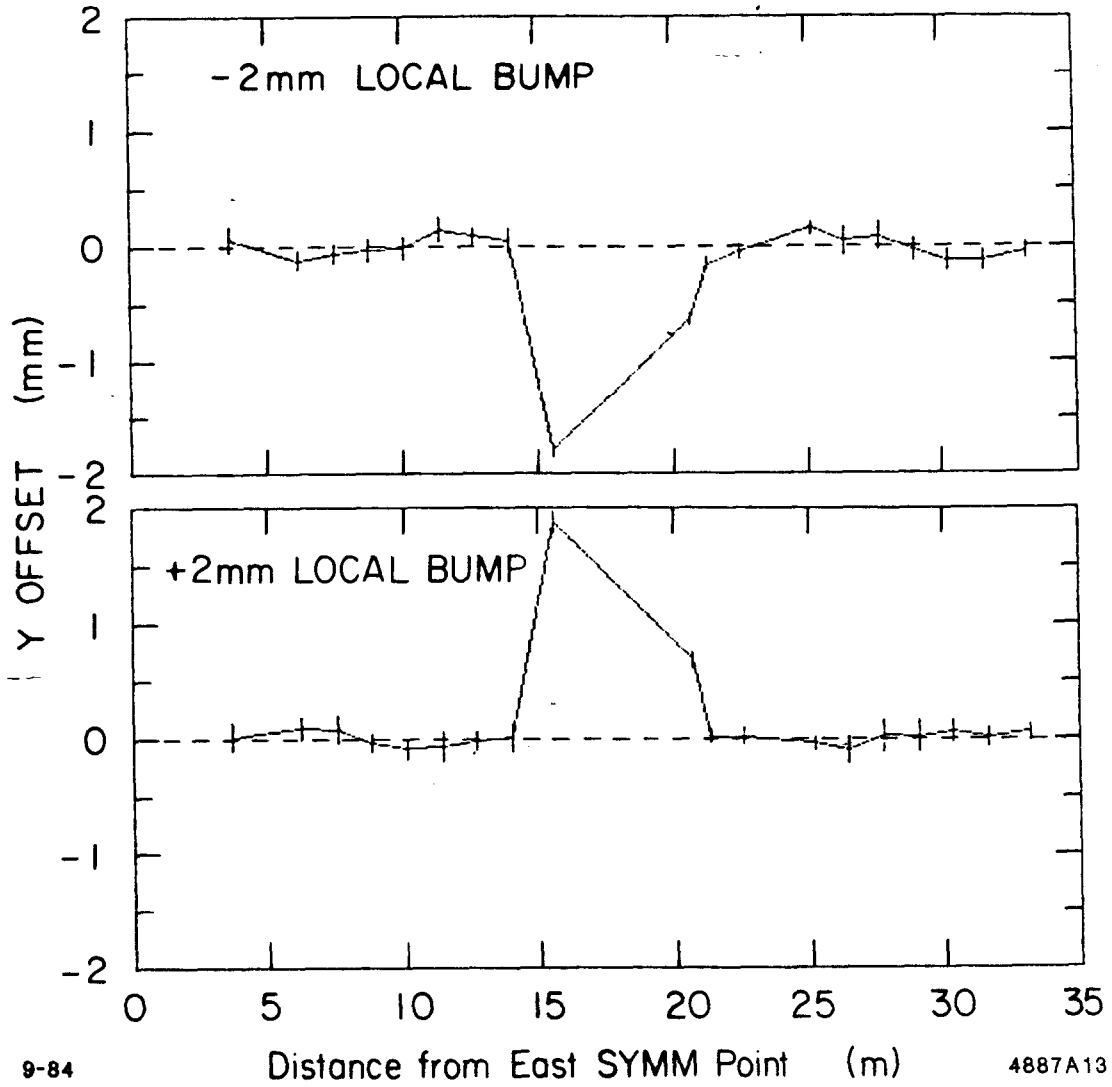
-2mm LOCAL BUMP
+2mm LOCAL BUMP
Y OFFSET (mm)
2
1
0
-1
-2
0
5
10
15
20
25
30
35
Distance from East SYMM Point (m)
9-84
4887A13

Fig. 13

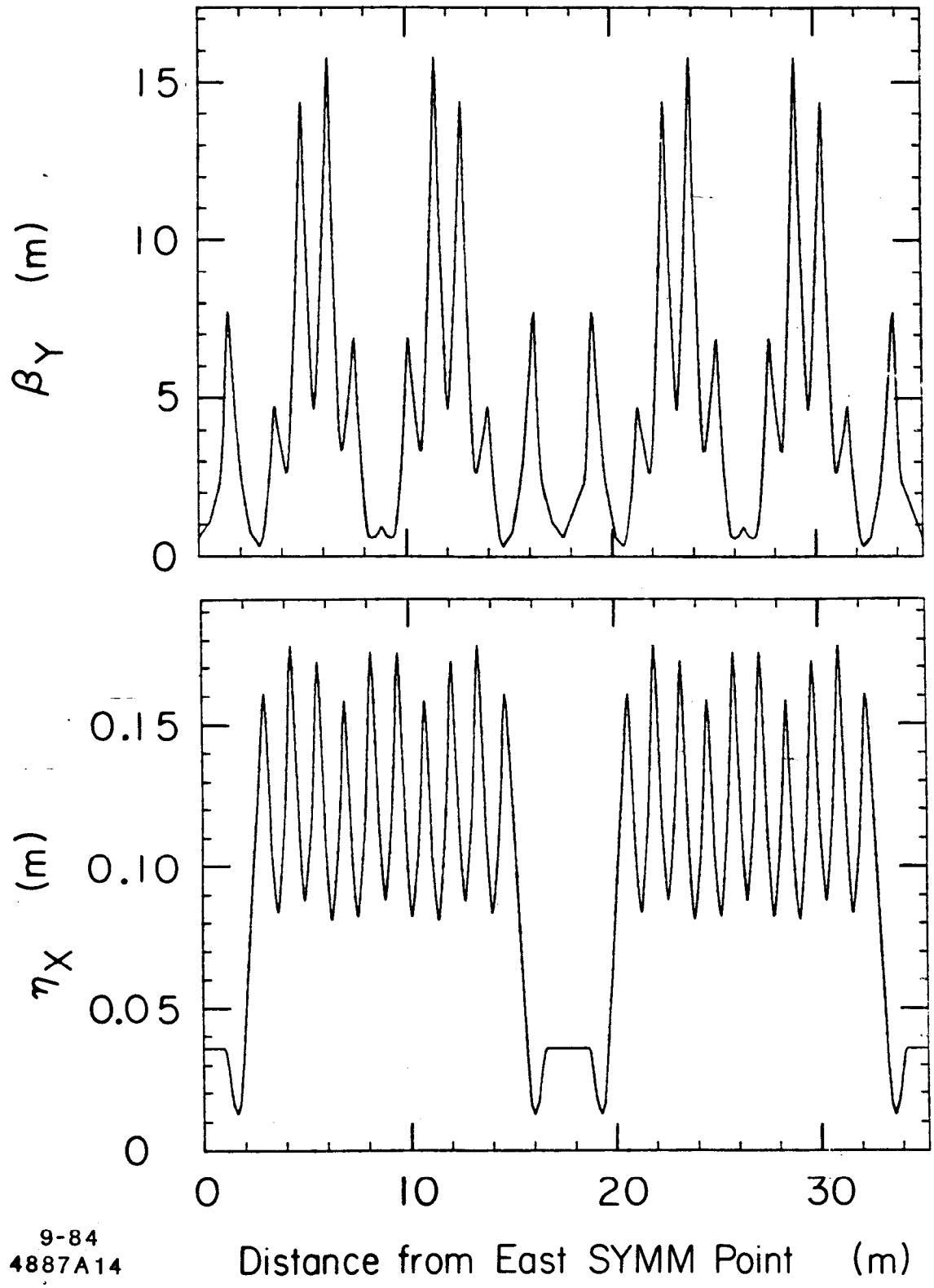
15
10
5
0
β_Y (m)
0.15
0.10
0.05
0
η_X (m)
0
10
20
30
Distance from East SYMM Point (m)
9-84
4887A14

Fig. 14

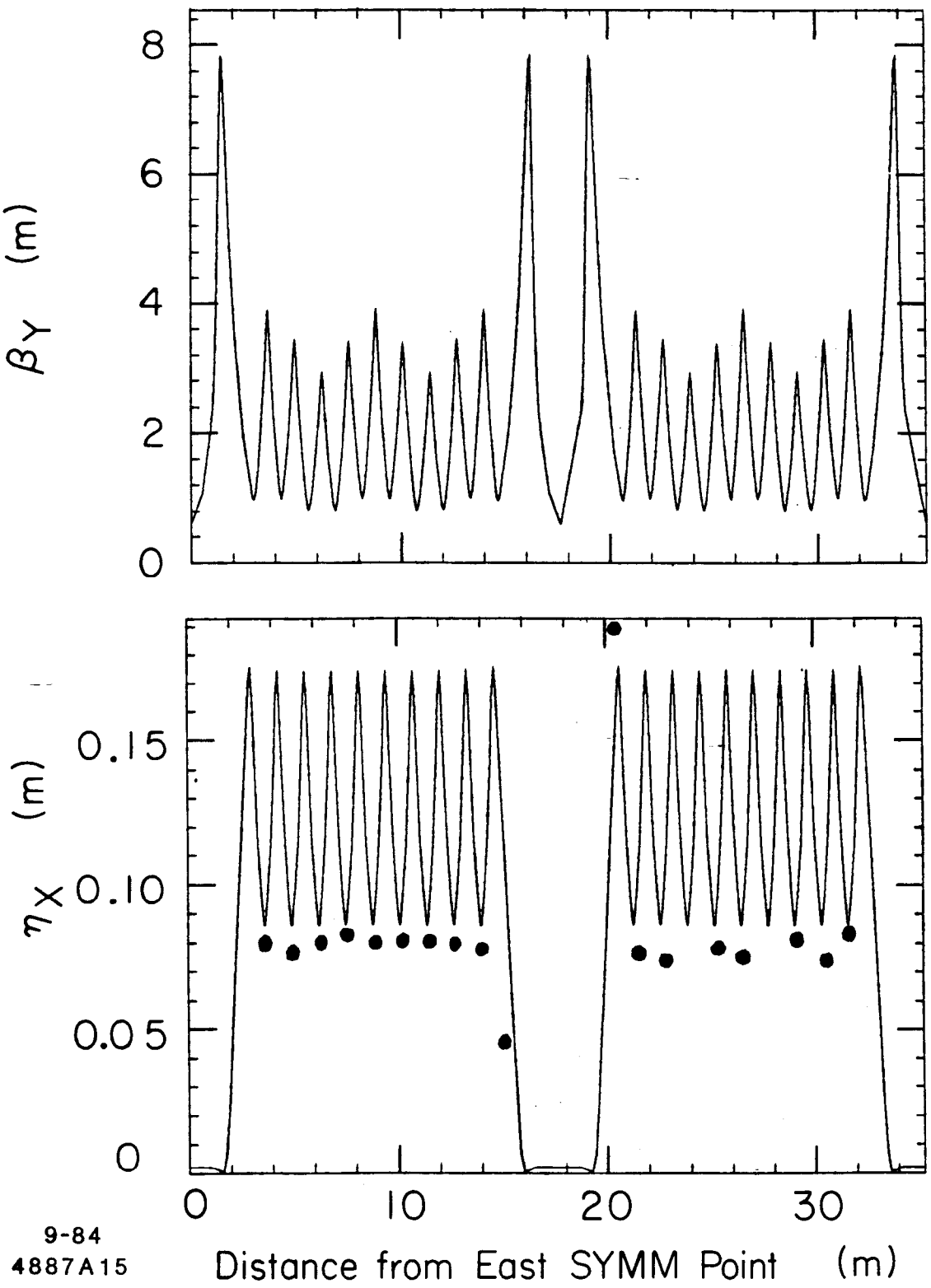
8
6
4
2
0
β_Y (m)
0.15
0.10
0.05
0
η_X (m)
0
10
20
30
Distance from East SYMM Point (m)
9-84
4887A15

Fig. 15

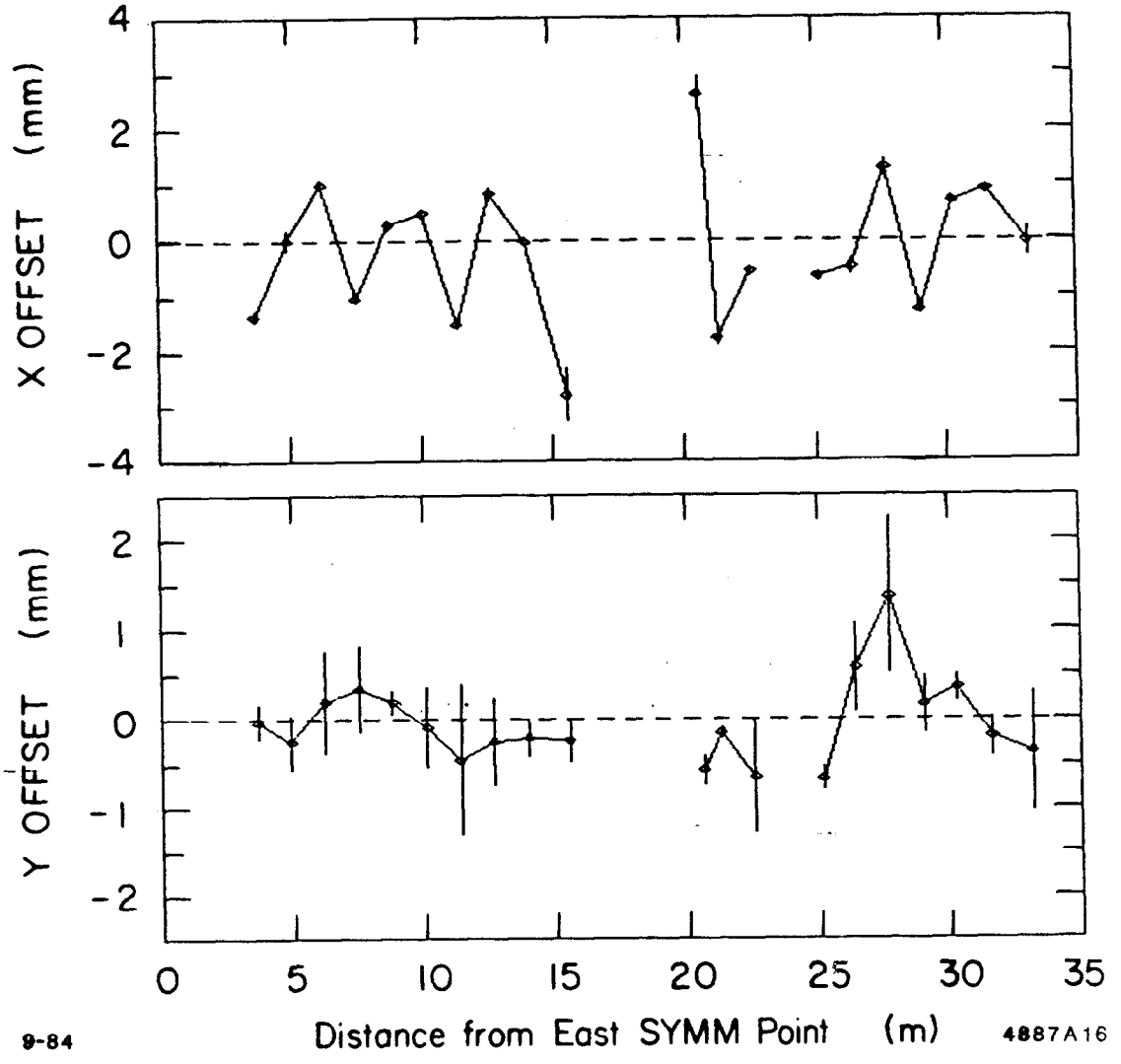
X OFFSET (mm)
4
2
0
-2
-4
Y OFFSET (mm)
2
1
0
-1
-2
0
5
10
15
20
25
30
35
Distance from East SYMM Point (m)
9-84
4887A16

Fig. 16